catalysts

MDPI

Article

Ethanol Dehydration to Ethylene over High-Energy Facets Exposed Gamma Alumina

Jiangang Lv [1], Di Wang [1], Luming Peng [2], Xuefeng Guo [2], Weiping Ding [2] and Weimin Yang [1,*]

[1] SINOPEC Shanghai Research Institute of Petrochemical Technology Co., Ltd., Shanghai 201208, China; lvjg.sshy@sinopec.com (J.L.)
[2] Key Lab of Mesoscopic Chemistry, The School of Chemistry and Chemical Engineering, Nanjing University, Nanjing 210093, China
* Correspondence: yangwm.sshy@sinopec.com

Abstract: Highly efficient and stable catalysts are among the key factors in industrial ethanol dehydration to ethylene. Among the widely studied catalysts, alumina is the most suitable for industrial application. In this study, novel gamma alumina was synthesized by solvent protection and a hydrothermal procedure. HRTEM, XRD, FT-IR, NH_3-TPD, H-D exchange, and ^{29}Si MAS NMR were employed to compare the difference in physicochemical properties between the novel gamma alumina and commercial alumina. Characterization results show that the as-synthesized novel gamma alumina mainly exposes the high-energy crystal plane (111) while the commercial alumina mainly exposes the thermostatically stable (110) crystal plane. The dominating (111) plane, according to the characterizations, endows the novel gamma alumina with a higher density of surface hydroxyl groups, higher acid content, and higher surface energy compared to the commercial alumina. The catalytic performance of the two catalysts for industrial ethanol dehydration to ethylene was studied. The novel (111) plane-exposed alumina showed a higher yield of ethylene than commercial alumina under the same reaction conditions. This could be related to the difference in atomic arrangement and the unsaturated aluminum coordination of different crystal planes. Stability testing under severe reaction conditions (450 °C, 1 MPa, 4 h^{-1}) indicates that novel gamma alumina shows better stability (catalyst life cycle increased by 50%) and produces less acetaldehyde as a byproduct. The effects of steam treatment on the catalytic performance were further investigated. The surface acidity and the catalytic performance of novel gamma alumina present a volcanic curve with the increase in steam treatment temperature. Under the optimal water vapor treatment temperature of 650 °C, the conversion of ethanol and selectivity of ethylene were both higher than 99%.

Keywords: alumina; ethanol dehydration; crystal plane regulation; hydrothermal treatment

check for updates

Citation: Lv, J.; Wang, D.; Peng, L.; Guo, X.; Ding, W.; Yang, W. Ethanol Dehydration to Ethylene over High-Energy Facets Exposed Gamma Alumina. *Catalysts* **2023**, *13*, 994. https://doi.org/10.3390/catal13060994

Academic Editor: Eric M. Gaigneaux

Received: 17 May 2023
Revised: 7 June 2023
Accepted: 7 June 2023
Published: 12 June 2023

Copyright: © 2023 by the authors. Licensee MDPI, Basel, Switzerland. This article is an open access article distributed under the terms and conditions of the Creative Commons Attribution (CC BY) license (https://creativecommons.org/licenses/by/4.0/).

1. Introduction

Ethylene is one of the most important raw materials in the petrochemical industry, and its production has been considered an indicator to measure the development level of national industry. According to China's 14th Five-Year plan, China will become the world's largest ethylene producer, with its production capacity increasing from 35.2 Mt in 2020 to 73.5 Mt by 2025 [1]. In China, ethylene is commonly produced by naphtha cracking (74%) and coal or the methanol-to-olefins process (20%), while ethane dehydrogenation accounts for the largest proportion of ethylene production in the Middle East and the United States [2]. Dwindling fossil fuels and the uneven distribution of petroleum in regions have driven the urgent need to develop alternative renewable feed stocks. In addition, the carbon neutrality policy [3] committed to by the Chinese government also calls for an ethylene production process that is less energy-intensive and creates fewer carbon emissions.

In the past decades, ethanol production from renewable biomass has been well developed; examples include the production of bioethanol from cyanobacteria [4], industrial

waste gas utilization to produce ethanol by biological fermentation [5], hydrogenation of CO_2 or CO to produce alcohols [6,7], and the break-through of coal-derived ethanol by the methanol dehydrogenation–DME carbonylation–methyl acetate hydrogenolysis pathway [8,9]. These technologies significantly reduce the price of ethanol and thus endow the process of ethanol dehydration to ethylene with great economic competitiveness (especially compared with the methanol-to-olefins route) and new application prospects [10]. Dehydration of ethanol to ethylene is an acid-catalyzed endothermic reaction with certain products and reactants. Theoretically, increasing the reaction temperature and decreasing the reaction pressure can effectively improve the conversion rate. Therefore, the key point for industrial ethanol dehydration to ethylene is to obtain higher selectivity and reaction stability through catalyst development [11,12]. Extensive studies have been carried out to develop heterogeneous catalysts for the dehydration of ethanol, including alumina [13–16], zeolites [17–19], metal oxides [20,21], and heteropoly acids [22,23]. Outstanding catalysts such as zeolite and heteropoly acid present high selectivity and lower reaction temperature when applied to ethanol dehydration at the laboratory scale, yet problems such as the short catalyst life and the narrow range of reaction temperatures need to be solved. Alumina, due to its impressive selectivity and stability, as well as its low cost, is regarded as the most suitable catalyst for industrial ethanol dehydration to ethylene [24]. Previous studies have been conducted on the preparation and characterization of γ-Al_2O_3 [25–28]; a few of these focus on crystal plane regulation of industrial gamma alumina and the relationship between surface properties and catalytic performance.

In this work, high-energy plane (111)-exposed gamma alumina was synthesized by solvent protection and a hydrothermal procedure. The differences in structural properties and surface acidity between the above alumina and conventional alumina, which mainly exposes the thermodynamically stable (110) crystal plane, were studied. Catalytic performance of the two catalysts for industrial ethanol dehydration to ethylene in a fixed-bed reactor was compared. Experimental results demonstrated that the novel (111) plane-exposed γ-Al_2O_3 shows higher activity, higher selectivity of ethylene, and higher reaction stability. Various characterizations were employed to describe the relationship between crystal plane exposure and the physicochemical properties of alumina, which inspired a novel strategy to design highly efficient catalysts by manipulating crystal planes.

2. Results and Discussion

2.1. Characterizations

2.1.1. Morphology and Textural Properties

High-energy plane (111)-exposed gamma alumina (HT-γ-Al_2O_3) was synthesized and compared with common commercial alumina (C-γ-Al_2O_3).

A high-resolution transmission electron microscope (HRTEM) was employed to detect the morphology of the two alumina samples. As shown in Figure 1a, the as-synthesized HT-γ-Al_2O_3 presents uniform nanorods with diameters of 7–8 nm and lengths of 60–100 nm. In our previous study [29–31], a reasonable three-dimensional model of gamma alumina was constructed according to theoretical calculations, in which the (111) crystal plane and (100) crystal plane alternately formed an octagonal structure at the cross section. The lattice spacing on the section was 0.460 nm, and the plane that presented an angle of 60° with the lattice fringe was discriminated as the (111) crystal plane. It can be deduced that the synthesized HT-γ-Al_2O_3 displayed the (111) crystal plane on the external surface, which increases the ratio of the (111) plane on alumina. This is due to the existence of the surfactant oleic acid, which effectively protects the high-energy (101) plane of AlOOH (see Table S1), and subsequently transforms to the corresponding (111) plane of gamma alumina by calcination (scheme shown in Figure S1). By comparison, as shown in Figure 1b, conventional alumina C-γ-Al_2O_3 showed an irregular porous structure formed by stacking of small particles. In addition, selected area electron diffraction (SAED) were carried out and the results were shown in Figure S2. Diffraction rings of (400) and (440) planes

are observable in the SAED patterns, and spots ascribed to (222) can be discriminated in Figure S2a.

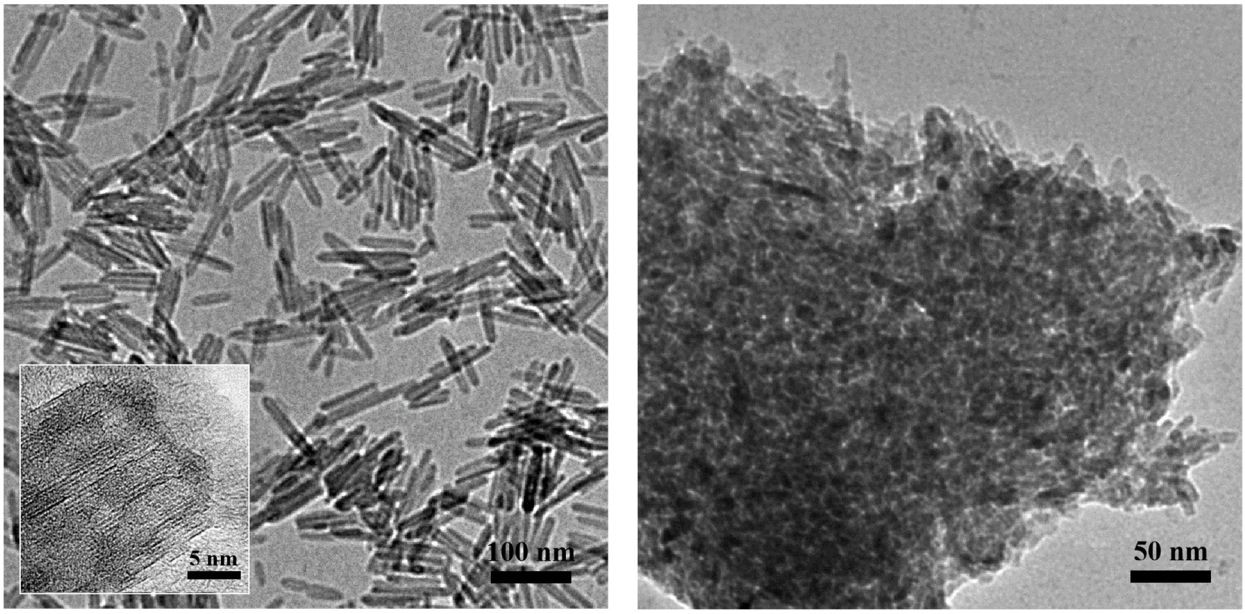


Figure 1. HRTEM images of the two alumina samples (**a**) HT-γ-Al_2O_3 and (**b**) C-γ-Al_2O_3.

X-ray diffraction (XRD) was used to analyze the crystal phase of the two samples, and the results are shown in Figure 2. Diffraction peaks at 37.6°, 45.8°, and 67.0° can be discriminated, corresponding to the characteristic peaks of gamma alumina (JCPDS No. 10-0425). In addition, HT-γ-Al_2O_3 has a narrow half-peak breadth and higher diffraction peak intensity than C-γ-Al_2O_3, indicating a higher crystallization degree and more regular morphology. This has good consistency with the HRTEM results.

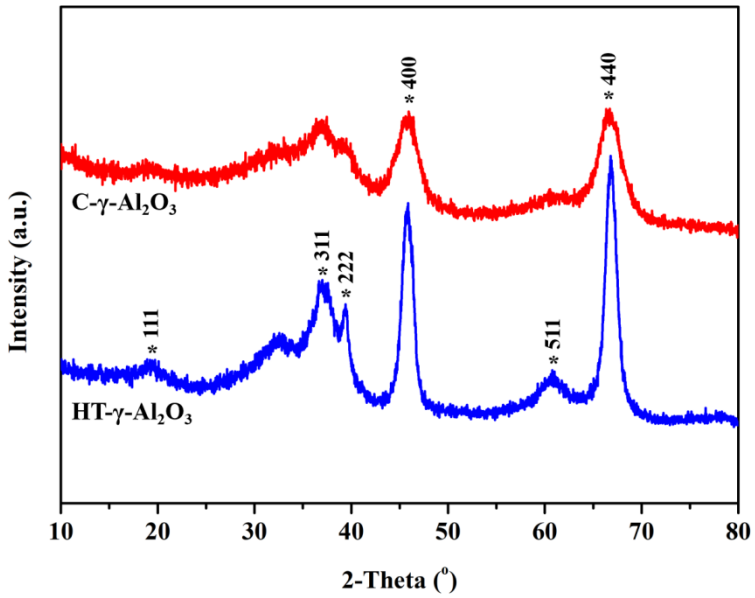


Figure 2. XRD patterns of the two alumina samples.

It is reasonable to infer that the different morphologies of the two samples are closely related to the synthesis procedure, because HT-γ-Al_2O_3 underwent extra hydrothermal treatment before calcination. In order to investigate the effect of hydrothermal treatment on

HT-γ-Al_2O_3, textural properties were detected by N_2 adsorption and are listed in Table 1. Both of the N_2 adsorption–desorption isotherms possess type IV sorption curves according to the IUPAC classification, as is typical of mesoporous materials. There were H2 hysteresis loops within the range of relative pressure of $P/P_0 \approx 0.6$–0.9. The high relative pressure of capillary condensation could be associated with larger mesoporous pore size. The desorption branch shows a steep drop at medium pressure, reflecting ink-bottle-shaped pores with small orifices and large cavities. According to Table 1, the pore size of alumina after hydrothermal treatment increases (7.6 nm → 8.7 nm), while the specific surface area decreases (213 $m^2/g \rightarrow 208\ m^2/g$), indicating that alumina grows gradually during hydrothermal treatment. It is worth pointing out that HT-γ-Al_2O_3 still maintains a narrow pore distribution after hydrothermal treatment, and shows good thermal stability and potential for catalytic reaction.

Table 1. Textural properties of the two alumina samples.

Sample	Specific Surface Area (m^2/g)	Average Pore Diameter (nm)	Pore Volume (m^3/g)
C-γ-Al_2O_3	213	7.6	0.410
HT-γ-Al_2O_3	208	8.7	0.453

2.1.2. Surface Properties

In order to investigate surface functional groups on alumina, Fourier transform infrared spectroscopy (FT-IR) was performed. Generally speaking, low wavenumbers of alumina IR spectra could be assigned to Al-O vibration bands, and high wavenumbers (3850–3550 cm^{-1}) were caused by surface hydroxyl groups. The spectra of the two catalysts in the region of surface hydroxyl groups are presented in Figure 3.

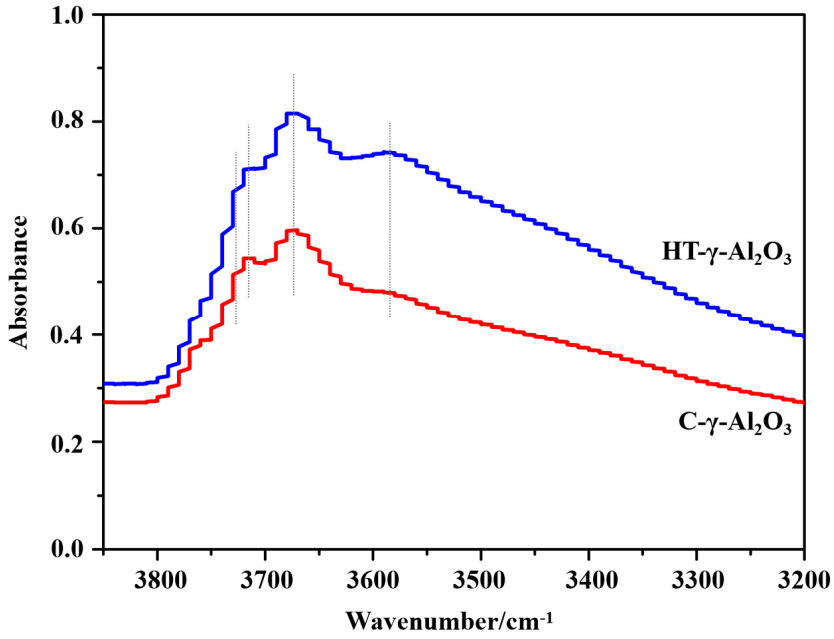


Figure 3. FT−IR spectra (the region of surface hydroxyl groups) of alumina catalysts.

In the range of 3850–3550 cm^{-1} there is a complex of 4–6 closely overlapped bands, which have been variously attributed to free or quasi-free surface OH groups. The different intensities usually imply the distinction in morphology (different exposed planes, corners, and edges), structure, or the quantity and type of impurities [32,33]. According to the spinel structure model of alumina and the hydroxyl model proposed by Knözinger et al. [34], there are five types of hydroxyl groups (types III, III, IIa, IIb, Ia and Ib) on alumina. Among

the above OH groups, type III and type IIa (band at 3730–3710 cm^{-1}) are characteristic hydroxyl groups on the (111) crystal plane [35], representing hydroxyl HO-μ_2-Al_{VI} and HO-μ_1-Al_{VI} (where Al_X stands for aluminum atoms surrounded by X oxygen atoms and HO-μ_n stands for OH groups linked to n aluminum atoms) on the (111) crystal plane, respectively. In addition, the characteristic hydroxyl groups on the (111) plane have the strongest charges among all hydroxyl groups. Therefore, the presence of type III and IIa hydroxyl groups predicts stronger surface Brønsted acidity.

Various studies have been carried out on the surface structure (hydroxyl group type, density, etc.) and surface properties of alumina [27,36,37]. For the low exponential surface (111), (110), and (100) planes of gamma alumina, the atomic arrangement and coordination number have a remarkable influence on the surface properties. According to the structural model proposed by Digne et al. [38,39], O and Al atoms appear alternately on the (111) crystal plane, penta-coordinated Al atoms and O atoms with triple coordination exist on the (100) crystal plane, while Al atoms with both quadruple and triple coordination, and two-coordinated and tri-coordinated O atoms appear on the (110) crystal plane. Theoretical calculation results (see Table S2) show that the order of both the number of Al-O bonds per unit area and energies of each Al-O bond is (111) > (110) > (100), and the surface energies of the contracted surfaces are 4480, 2590, and 1430 mJ/m^2, respectively; that is, among the low exponential planes of γ-Al_2O_3, the (111) crystal plane has the highest acid density and surface energy.

^{29}Si MAS NMR measurements were carried out to study the dispersion and interaction on the alumina surface, as shown in Figure 4. Before the characterization, 4 wt% SiO_2 (lower than the dispersion capacity of the alumina monolayer) was loaded on the two alumina samples. The resonance at −116 ppm was attributed to the crystallographically equivalent site of the $Si(OSi)_4$ (Q4) group, and resonance at −78 and −83 ppm can be assigned to $Si(OSi)_2(OH)_2$ and $Si(OAl)_3OH$, respectively [40]. As shown in Figure 4, Si species on the HT-γ-Al_2O_3 surface are mainly $Si(OAl)_3OH$ groups, reflecting less contact between Si species, whereas there are three kinds of Si species on the surface of C-γ-Al_2O_3, implying Si species are in the aggregation state; that is, HT-γ-Al_2O_3 has stronger interaction with surface species and better dispersion on the surface than conventional alumina C-γ-Al_2O_3. According to the above analysis, HT-γ-Al_2O_3 preferentially exposes the (111) crystal plane; hence, the strong interaction can be reasonably attributed to the higher surface energy of (111) crystal plane. In summary, Si species tend to form aggregates on the (110) crystal plane, while on the (111) crystal plane they tend to form monodisperse Si species, as shown in Figure 4b.

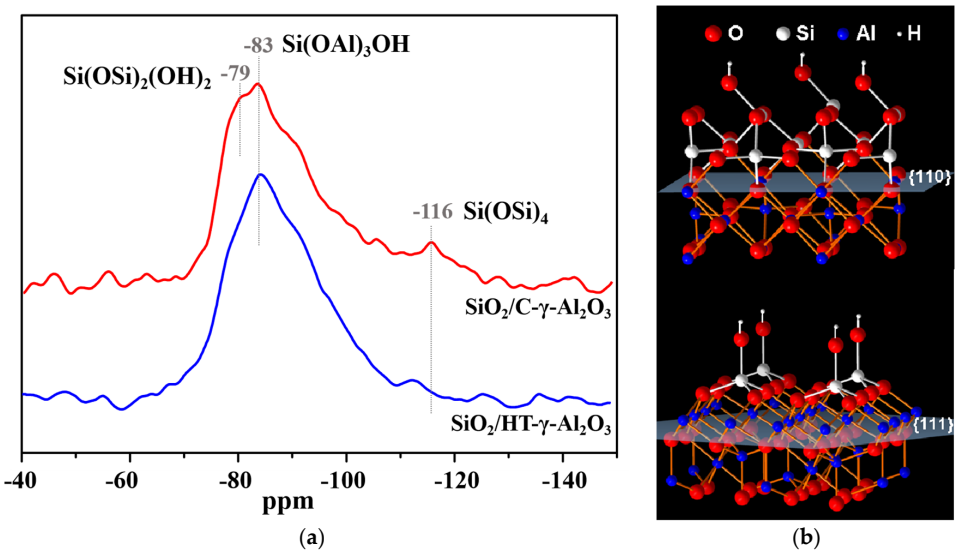
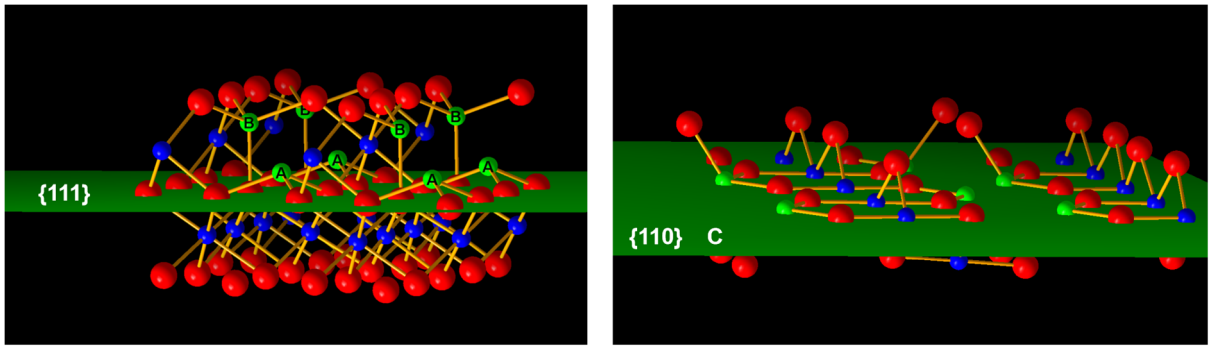


Figure 4. Dispersion on alumina surface. (**a**) ^{29}Si MAS NMR of 4%$SiO_2/\gamma-Al_2O_3$ and (**b**) dispersion of Si species on different crystal facets.

2.1.3. Acidity

The type and quantity of coordinative unsaturated aluminum on the surface are strongly related to the surface acidity. The coordinative unsaturated Al (Lewis acid) on the surface can provide a vacant orbital for the OH group, and the unsaturated O atom (Lewis base) with a lone-pair electron can accept a proton to form the OH group. H_2O absorbed on the alumina surface dissociates and is subsequently hydroxylated. The Lewis acid receives the OH group to form a Brønsted base, while the Lewis base receives a proton (from H_2O dissociation) to form a Brønsted acid. The hydroxylation and dehydration on the alumina surface are reversible. Generally, thermodynamically stable (less-active) crystal planes tend to be exposed first during crystal growth. For gamma alumina, the preferential crystal plane is (110). Tetra-coordinated Al atoms (layer C in Figure 5b) on the (110) crystal plane are dehydroxylated to form quasi-tri-coordinated Al. However, it will spontaneously enter the octahedral vacancy of the next layer to form hexa-coordinated Al, due to its high energy density and unstable geometry. For the (111) crystal plane, tetra-coordinated Al atoms (labeled A in Figure 5a) also form quasi-tri-coordinated Al by OH removal, but it can exist because of the relatively stable geometric configuration. In addition, the Al vacancy on the (111) crystal plane helps reduce the energy, making the quasi-tri-coordinated Al atoms stable. Under normal conditions, the lower the coordination number of aluminum, the stronger the Lewis acidity. In general, tri-coordinated Al on the alumina surface represents a strong acid center, tetra-coordinated Al means a medium-strong acid center, and penta-coordinated Al means a weak acid center. In summary, the (111) crystal plane has stronger Lewis acidity than the (110) crystal plane due to the presence of quasi-tri-coordinated aluminum.



(**a**) (**b**)

Figure 5. Diagram of surface atoms on (**a**) (111) facet (**b**) (110) facet of γ-Al_2O_3, where red spheres represent O atoms, and blue and green spheres represent Al atoms.

D_2-OH isotope thermally driven exchange was used to further characterize the surface hydroxyl density and Brønsted acid intensity of alumina. The activation energy for the exchange reaction $D_2 + OH \rightarrow OD + HD$ can be correlated with the O-H bond energy and the exchange is easier with a weaker O-H bond, as supported by DFT calculations [41], implying stronger acidic OH groups exchange with D_2 at lower temperatures. Hydroxyl density can be quantitatively determined after all H-D exchange is completed. The obtained H-D exchange curve is shown in Figure 6a. From the above analysis, the peak at the lower temperatures corresponds to the D_2 exchange with the acidic hydroxyl groups and the peak at the higher temperatures is the D_2 exchange with the non-acidic hydroxyl groups. HT-γ-Al_2O_3 possesses a larger number of acidic hydroxyl groups than C-γ-Al_2O_3, in accordance with the above structure analysis that shows that HT-γ-Al_2O_3 mainly exposes the (111) plane. According to mass spectrum results, the hydroxyl density of HT-γ-Al_2O_3 and C-γ-Al_2O_3 is 0.90×10^{15} and 0.62×10^{15} cm^{-2}, respectively. That means the hydroxyl density of alumina increases after hydrothermal treatment. In addition, the HT-γ-Al_2O_3 curve started to exchange at a lower temperature (250 °C), indicating that hydrogen in the

hydroxyl group on its surface was more easily dissociated. This further proves the stronger acidity of HT-γ-Al_2O_3, which is in good agreement with the FT-IR results.

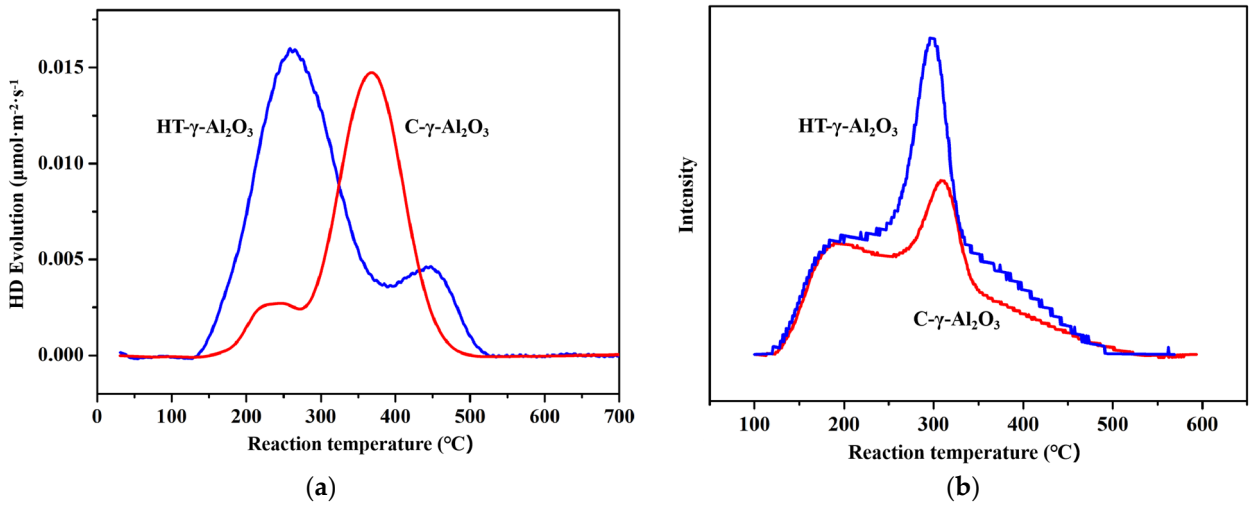


Figure 6. (**a**) H−D revolution profiles and (**b**) NH_3−TPD results of the two alumina catalysts.

NH_3 temperature-programmed desorption (NH_3−TPD) was employed to characterize the acid strength and acid content distribution on the surface of the two catalysts, as shown in Figure 6b. Both HT-γ-Al_2O_3 and C-γ-Al_2O_3 show two NH_3 desorption peaks that represent two kinds of acid center, where the low-temperature desorption peak represents a weak acid center, and the middle temperature desorption peak represents a medium-strong acid center. Considering the shoulder peak of ammonia desorption at ~350 °C, HT-γ-Al_2O_3 has higher acid density and acidity than the other samples. This verifies that the exposed surfaces of HT-γ-Al_2O_3 possess more dense acidic OH groups, which is a property of the (111) crystal plane. According to the peak area of NH_3 desorption, the weak acid content of the two alumina samples is basically the same, while the medium-strong acid content of HT-γ-Al_2O_3 (with hydrothermal treatment) increases significantly and shifts to a lower temperature, indicating an increase in total acid content and relatively constant acid strength. This kind of increase in non-strong acid will, in principle, improve the performance of HT-γ-Al_2O_3 as a catalyst for ethanol dehydration.

2.2. Ethanol Dehydration

2.2.1. Catalytic Performance

The two alumina catalysts were applied to the ethanol dehydration reaction to study their catalytic performance. In addition to the main product of ethylene, the reaction of ethanol dehydration also generates a small quantity of byproducts, such as diethyl ether, acetaldehyde, and hydrocarbons (methane, ethane, propylene, and C4). Extensive experiments [42,43] show that the byproduct is mainly diethyl ether at the lower conversion of ethanol, while it becomes C4 at high ethanol conversion. The ethanol dehydration reaction routes mainly involve three reversible reactions, namely, ethanol intramolecular dehydration to ethylene, ethanol intermolecular dehydration to diethyl ether, and diethyl ether dehydration to ethylene. As can be seen from Figure 7a, the yield of ethylene over the two catalysts increases with the increase in the reaction temperature, reaching complete conversion to ethylene at about 350 °C. Ethanol dehydration is a reversible reaction, of which the forward reaction is endothermic. Therefore, when raising the reaction temperature, the reaction equilibrium moves in the direction of the forward reaction, thus increasing the conversion rate of ethanol. In addition, reaction temperature has a significant influence on the product distribution. It favors ethanol intermolecular dehydration to form diethyl ether at a relatively low reaction temperature, while high temperature is conducive to the intramolecular dehydration of ethanol to form ethylene.

At a low reaction temperature, not only is conversion of ethanol lower, but more diethyl ether is also produced. The two aspects together lead to a low yield of ethylene. Therefore, adequate temperature is necessary for ethanol dehydration on alumina.

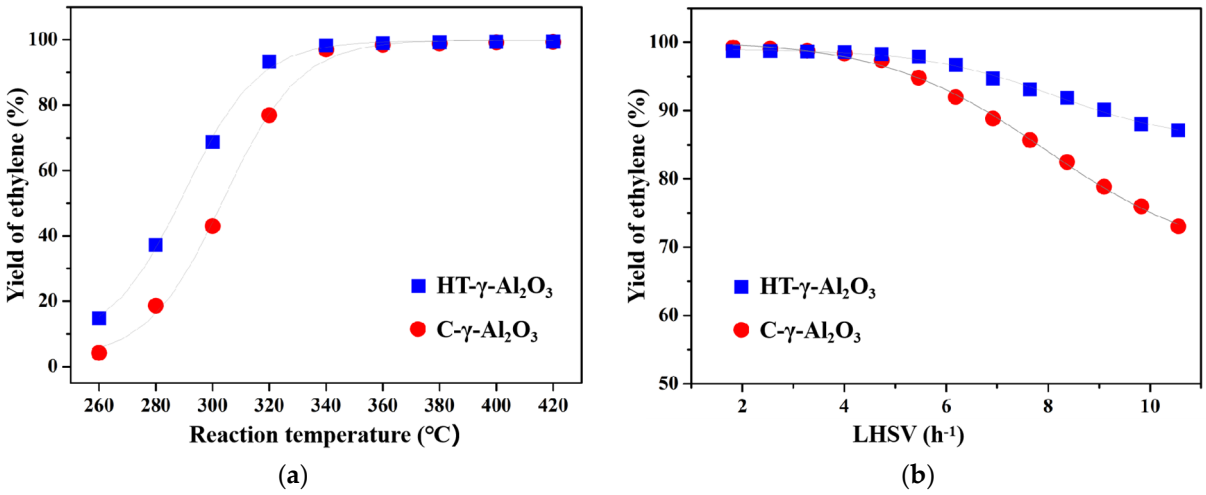


Figure 7. Catalytic performance of the two catalysts for absolute alcohol dehydration at (**a**) different reaction temperatures and (**b**) different LHSV.

It is worth noting that HT-γ-Al_2O_3 after hydrothermal treatment shows better low-temperature activity at the same LHSV, due to the stronger acidity on its surface. For example, at 300 °C, the yield of ethylene on HT-γ-Al_2O_3 is about 70%, while that on C-γ-Al_2O_3 is only 42%. Low-temperature activity is of great significance for industrial ethanol dehydration catalysts because the deactivation of the ethanol dehydration catalyst is usually caused by carbon deposits, which are significantly affected by the reaction temperature. On the acid center of alumina, the ethanol molecule is eliminated to intermediately form carbon, and then rapidly loses β-H to form alkenes. In the meantime, the series reaction of ethylene polymerization takes place and generates carbon deposits [11]. With an increase in the reaction temperature, the rate of polymerization series reaction increases and the carbon accumulation rate accelerates. As a result, the surface area, pore volume, and acidity of catalysts will decrease, leading to final deactivation. It can be deduced that if one catalyst possesses excellent low-temperature activity, it means that the catalyst could operate at a lower reaction temperature, thus slowing down carbon deposit and extending the catalyst's life. Therefore, HT-γ-Al_2O_3 shows greater potential as a catalyst for industrial ethanol dehydration due to its excellent low-temperature activity.

The key step of ethanol dehydration to ethylene on an alumina catalyst is ethanol's interaction with the surface Brønsted acid site (Al-OH) to form ethoxy intermediates [44], in which the surface OH group plays an important role. An in situ infrared experiment of ethanol dehydration showed that in the initial stage of the reaction, the disappearance of OH groups and emergence of ethoxy groups occurred simultaneously [26]. A part of ethanol formed ethoxy groups and H_2O by replacing OH groups on the alumina surface, while another part of ethanol tended to form ethoxy groups and new OH groups by dissociation and adsorption on Lewis acid–base pairs. Surface ethoxy groups are the intermediate stage to producing both ethylene and diethyl ether.

Typical product distributions on alumina at different conversion levels are listed in Table 2. There was almost no diethyl ether at high conversion (~99%), but a certain amount of diethyl ether (9.14%) appeared at the medium conversion level. Since the reaction order of diethyl ether synthesis is higher than that of ethanol dehydration to ethylene [45], the partial pressure of reactant ethanol becomes an important issue. It is generally believed that diethyl ether is formed through nucleophilic substitution reaction, in which the ethoxy group acts as a nucleophilic reagent and interacts with another ethanol molecule to increase

the electrophilicity of the alcohol carbon atom, and further nucleophilic substitution to form diethyl ether (reversible reaction). When fewer ethanol molecules are available (i.e., high conversion level of ethanol), the reversible reaction disappears and the reaction of ethylene production dominates.

Table 2. Typical product distribution (%) at different conversion levels.

	Ethylene	Ethane	Propylene	Acetaldehyde	C4	Ethanol	Diethyl Ether	Others
High conversion	99.77	0.12	0.01	0.01	0.07	0.00	0.01	0.00
Medium conversion	90.20	0.29	0.04	0.02	0.10	0.16	9.14	0.03

The effect of different space velocities on catalytic performance (reaction temperature 350 °C) was further investigated, as shown in Figure 7b. The yield of ethylene decreased significantly with the increase in space velocity. On one hand, the short residence time of ethanol and the limited contact with active sites at a high space velocity are responsible for decreasing conversion. On the other hand, as the conversion level decreases, it produces more diethyl ether, as mentioned above, which, overall, decreases the yield of ethylene.

In addition, the yield of ethylene decreases more slowly on HT-γ-Al_2O_3 than C-γ-Al_2O_3 with the increase in space velocity, making HT-γ-Al_2O_3 a potential catalyst for industrial ethanol dehydration at a high space velocity. This is because HT-γ-Al_2O_3 mainly exposes the (111) crystal plane and thus presents more edge sites than C-γ-Al_2O_3, which mainly exposes the (110) crystal plane [46]; in addition, OH groups and coordinated unsaturated aluminum on different crystal planes result in different acid strengths [34]. The two aspects together affect product distribution on the HT-γ-Al_2O_3 catalyst. According to H-D exchange and NH_3-TPD, the HT-γ-Al_2O_3 catalyst possesses higher density of OH groups and stronger acidity, leading to the stronger adsorption strength of ethanol on the surface and forming more ethoxy intermediates, which are conducive to the formation of ethylene.

2.2.2. Stability

In addition to reactivity and selectivity, long period stability is another important index of catalysts for industrial ethanol dehydration to ethylene. The stability of the two catalysts was tested under severe conditions (450 °C, 1 MPa, 4 h^{-1}) with industrial ethanol (95%) as reactant. Changing curves of product ethylene and the main byproduct acetaldehyde are shown in Figure 8. HT-γ-Al_2O_3 shows better stability (catalyst life cycle increased by 50%), and produces less acetaldehyde byproduct. In addition, as previously mentioned, HT-γ-Al_2O_3 has greater low-temperature activity and can operate stably at a lower temperature, resulting in an improvement in catalyst life of more than 50%.

The adsorption–desorption of H_2O and ethanol is competitive. When the reaction temperature is fixed, theoretically, the difference in the degree of hydroxylation between two alumina surfaces will gradually weaken or even disappear as the desorption of reactant H_2O and the re-adsorption of the generated H_2O reaches an equilibrium. However, based on results in Figure 8, the selectivity of ethylene and acetaldehyde on the two catalysts varies significantly, which is caused by the different acid distributions on the surface. According to mechanism studies [47], ethanol dehydrogenates to acetaldehyde at basic sites and dehydrates directly or via diethyl ether to ethylene at acidic sites. Because of the strong acidity and higher total acid content of HT-γ-Al_2O_3, the reaction of ethanol dehydration to ethylene always dominates on the surface.

It is generally believed that the byproduct C4 is produced through ethylene dimerization. On one hand, strong acid sites of the catalyst should be strengthened in order to decelerate C4 production, due to the lower polymerization rate of ethylene at strong acid sites. On the other hand, however, excessive strong acid will accelerate deactivation, because the strong acid center is the active center of the carbon deposit. Therefore, in order to design selective and stable catalysts for ethanol dehydration, the appropriate amount

of medium-strong acid is an important consideration. The above experimental results are consistent with NH_3-TPD. The amount of medium-strong acid on HT-γ-Al_2O_3 after hydrothermal treatment increases, endowing HT-γ-Al_2O_3 with higher product selectivity and reaction stability.

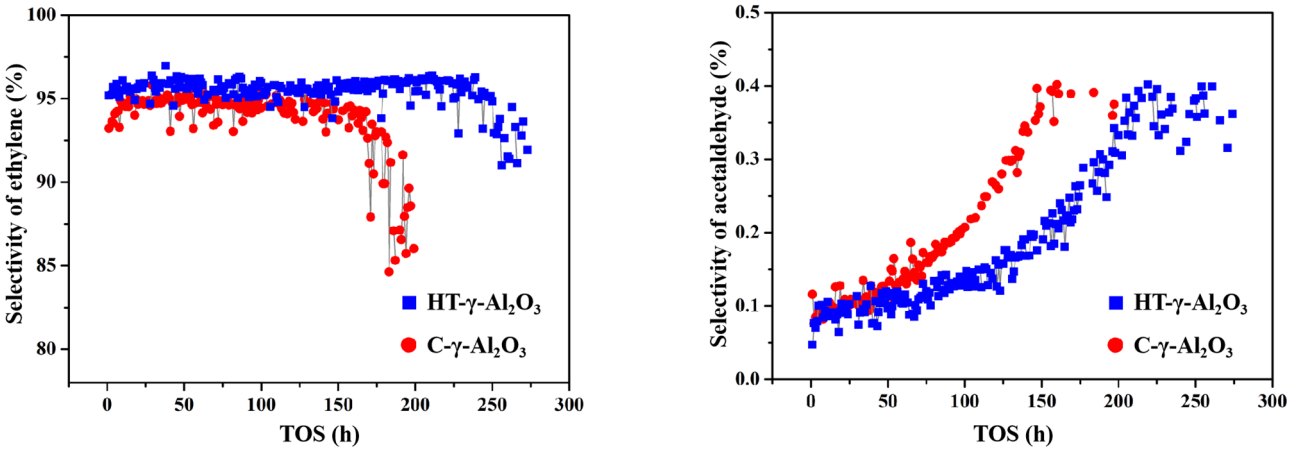


Figure 8. Stability test under severe conditions (450 °C, 1 MPa, 4 h^{-1}) with industrial ethanol as reactant: selectivity of (**a**) ethylene and (**b**) byproduct acetaldehyde.

2.2.3. Effect of Steam Treatment

Steam treatment is considered an effective way to adjust the physicochemical properties of the alumina surface. In order to further improve the catalytic performance, the aforementioned selective and stable HT-γ-Al_2O_3 was treated with water vapor at different temperatures for 3 h. The treated alumina catalysts were applied to a 95% ethanol dehydration reaction at a low temperature (320 °C), and the catalytic performance is shown in Table 3. When HT-γ-Al_2O_3 was treated in steam at 650 °C, the catalytic performance significantly improved, resulting in conversion of ethanol and selectivity of ethylene that were both higher than 99%. The catalytic performance of HT-γ-Al_2O_3 compared with catalysts from the literature is listed in Table 4. Comprehensively considering the effect of reaction temperature and ethanol purity, catalysts in this work show the highest activity for ethanol dehydration to ethylene.

Table 3. Effect of steam treatment temperature on catalytic performance of HT-γ-Al_2O_3.

	HT-γ-Al_2O_3	Steam Treatment Temperature/°C			
		500	650	800	900
Conversion of ethanol %	96.0	98.2	99.9	97.2	98.0
Selectivity of ethylene %	94.0	96.4	99.6	95.3	95.1

Table 4. Comparison with catalysts from references.

Catalyst	HT-γ-Al_2O_3	HT-γ-Al_2O_3 −650 °C Treated	Industrial Alumina	Silica-Alumina	SiO_2-ZrO_2	Phospho-molybdic Acid-PILC	ZSM-5 Nanosheets
Reactant ethanol	absolute	95%	94%	absolute	99.5%	absolute	bioethanol
Temperature (°C)	350	320	400	400	450	300	300–350
Conversion%	100	99.9	97.5	100	99.2	93.2	>90
Selectivity of ethylene%	99.8	99.6	95.0	96.1	96.7	99.1	85%
Reference	This work	This work	24	13	21	22	17

The effect of steam treatment on physicochemical properties and Al atom migration of alumina was investigated by XRD. For comparison, C-γ-Al_2O_3 was also treated with water vapor under the same conditions, and the XRD patterns of the two catalysts after steam treatment are shown in Figure 9.

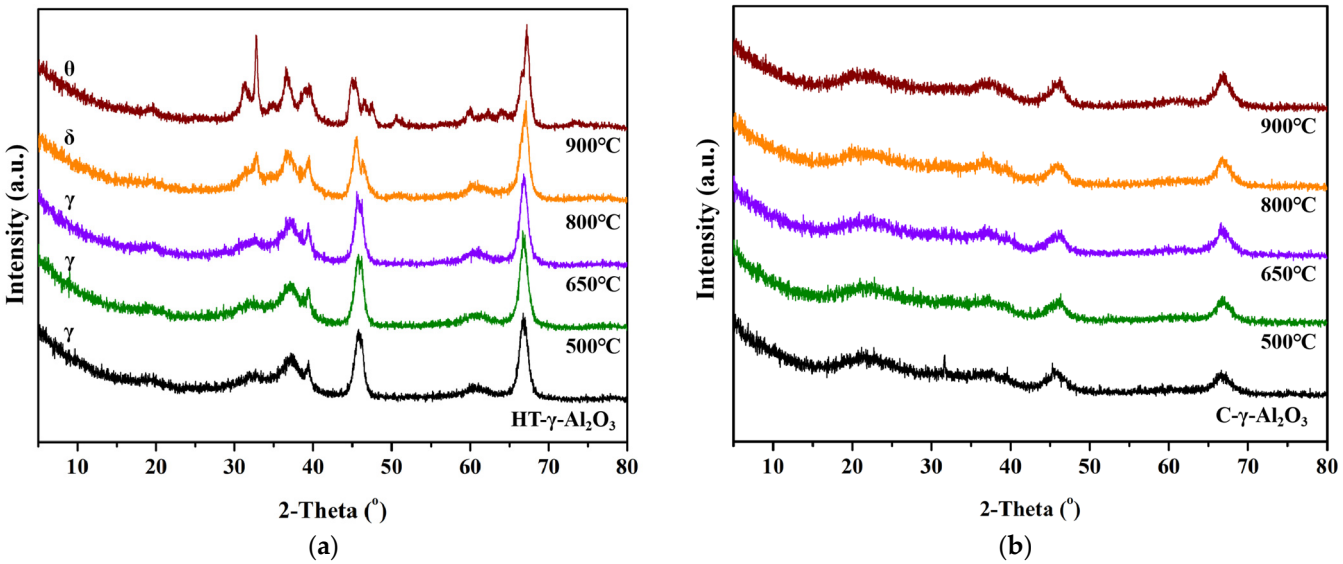


Figure 9. XRD patterns of (**a**) HT-γ-Al_2O_3 and (**b**) C-γ-Al_2O_3 treated at different temperatures in steam.

As shown in the XRD patterns, the crystal size of both types of alumina did not change significantly after high-temperature treatment. With the increase in the steam treatment temperature, the crystal structure of HT-γ-Al_2O_3 changes obviously. For example, δ-phase occurred after the 800 °C treatment and θ-phase was detected after the 900 °C treatment, while C-γ-Al_2O_3 did not show a phase transformation. This phenomenon could be ascribed to different surface energies of different crystal planes. C-γ-Al_2O_3 with the (110) crystal plane shows a lower surface energy, and will remain stable at high temperature. HT-γ-Al_2O_3 mainly exposes the high-energy (111) crystal plane and tends to transfer into a more stable state at high temperature, resulting in the phase transformation during steam treatment. In the environment of water vapor, OH groups around the Al atom form a large number of intramolecular and intermolecular hydrogen bonds with H_2O. The bond energy of the Al-O bond is weakened due to the existence of these hydrogen bonds, and breaks at high temperature, causing migration or removal of hexa-coordinated Al. As a result, the stacking mode between Al-O atoms changes and thus affects the distribution of surface acidity. According to BET characterization results, the specific surface area showed a decreasing trend with the increase in steam treatment temperature, but the pore structure of alumina did not change significantly. This is because only Al^{3+} local migration occurred during the transformation from γ-phase to θ-phase, while the O^{2-} did not rearrange.

To analyze surface acidity of HT-γ-Al_2O_3 treated at different temperatures, NH_3-TPD experiments were performed and results are shown in Figure 10. With the increase in the steam treatment temperature from 550 °C to 650 °C, the acid density per unit mass ought to decrease because of the decreasing specific surface area, but the acid density (peak area) actually increases in Figure 10. Based on the theoretical calculation of OH groups' desorption on different alumina crystal planes, the binding energy of the OH groups on the (111) plane is higher than that on other planes. Therefore, desorption of OH groups on the (111) crystal plane requires a higher temperature. Only if the steam treatment temperature rises to 650 °C will a large number of OH groups remove from the surface, thus resulting in increased acid content. When the steam treatment temperature further increases to a high temperature (900 °C), total acid content decreases due to the decreasing surface area, and

the catalytic performance of ethanol dehydration obviously decreases (Table 3). Based on the above results, the optimal steam treatment temperature was determined as 650 °C.

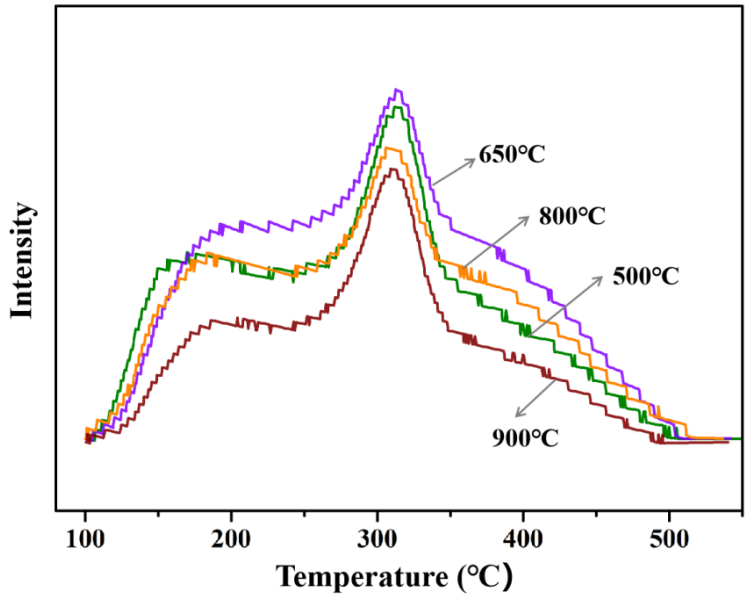


Figure 10. NH_3-TPD of HT-γ-Al_2O_3 catalyst treated at different temperatures in steam.

3. Materials and Methods

3.1. Materials

Oleic acid ($C_{18}H_{34}O_2$, AR, Sigma-Aldrich, St. Louis, MO, USA), boehmite colloidal particulates (AlOOH, CP, Zhejiang Yuda Chemical Co., Ltd., Ningbo, China), ammonia ($NH_3 \cdot H_2O$, AR, Sinopharm Chemical Reagent Co., Ltd., Shanghai, China), absolute ethanol (C_2H_6O, AR, Aladdin Holdings Group Co., Ltd., Shanghai, China), and ethanol (C_2H_6O, 95%, Aladdin Holdings Group Co., Ltd., Shanghai, China) were all purchased from commercial sources.

3.2. Catalyst Synthesis

The typical procedure to synthesize novel alumina was described in detail in our previous work [29–31]. Quantities of 5 g of oleic acid and 60 g of boehmite colloidal particulates were dispersed in deionized water under magnetic stirring at 80 °C. An appropriate amount of ammonia was added drop-wise into the mixture to adjust pH to ~8.5. After stirring overnight, the mixture was transferred into a Teflon-lined stainless steel autoclave and heated to 150 °C for 48 h. After cooling to room temperature, the solid precipitate was collected by centrifugation, rinsed with absolute ethanol several times, and dried at 80 °C. The precursor powder was then calcined at 550 °C for 4 h to obtain the final product, denoted as HT-γ-Al_2O_3 (where HT stands for hydrothermal). For comparison, industrial γ-Al_2O_3 was acquired from SINOPEC Shanghai Research Institute of Petrochemical Technology Co., Ltd. and denoted as C-γ-Al_2O_3 (where C stands for commercial). The C-γ-Al_2O_3 sample was also calcined at 550 °C for 4 h.

3.3. Characterizations

The morphology of the samples was examined using a JEOL JEM-2010 high-resolution transmission electron microscope (HRTEM, Tokyo, Japan), operated at an accelerating voltage of 200 kV.

X-ray powder diffraction (XRD) was performed on a Philips X'pert Pro diffractometer (Amsterdam, Netherlands) using Cu-Kα radiation (λ = 0.15418 nm) generated at 40 kV and 40 mA, with a scanning range from 10° to 80° at a speed of 0.02°/s.

The specific surface area and pore size distribution of the samples were measured by nitrogen adsorption using a Micromeritics ASAP-2020 analyzer (Norcross, GA, USA). Before the analysis, the samples were degassed for sample preparation at 120 °C in a vacuum for 1 h. The specific surface area was calculated according to the Brunauer–Emmett–Teller (BET) model. The total pore volume and pore size distribution were evaluated using the Barrett–Joyner–Halenda (BJH) method.

NH_3-TPD profiles were obtained using a BEL-CAT-B-82 apparatus (Osaka, Japan) equipped with a thermal conductivity detector (TCD) and mass spectrum (MS). Prior to the adsorption of NH_3, a 0.1 g sample was pretreated in He flow at 600 °C (20 °C/min) for 30 min and then cooled to 100 °C. The sample was then saturated with a 5% NH_3/He stream at 100 °C for 30 min. Then the excess ammonia was removed by He. Ammonia gradually desorbed by heating from 100 °C to 600 °C at a rate of 10 °C/min.

Fourier transform infrared spectroscopy (FT-IR) was undertaken using a Nicolet 5700 spectrometer (Waltham, MA, USA) equipped with a KBr beam splitter. A quantity of 50 mg of sample powder (dried, 200 mesh) was pressed into a transparent sheet on a tablet press for measurement. Before the characterization, samples were pretreated under vacuum at 300 °C for 0.5 h. The FT-IR setup and procedures used were detailed in the literature [48,49]. The spectra were collected with a 4 cm^{-1} resolution in 4000–1300 cm^{-1} and 32 scans were accumulated for each spectrum.

H-D exchange was used to characterize the surface hydroxyl density. The catalyst samples (400 mg) were pretreated in He at 600 °C (10 °C/min) for 1 h and then cooled to room temperature. The deuterium (6%D_2/Ar) exchanged with protonium presented in the samples was measured by increasing the temperature to 700 °C (10 °C/min). The signal of HD molecules was monitored by mass spectrometry. Ar was used as an internal standard to calculate the formation of HD during the exchange between D_2 and hydroxyls in the samples. The density of hydroxyl groups on the surface was calculated by detecting the final exchanged H-D amount at equilibrium and according to the quantitative relation of $D_2 + OH \rightarrow OD + HD$. The H-D exchange setup and procedures used were detailed in the literature [50,51].

^{29}Si MAS NMR was determined using a Bruker Avance Type III pulsed solid state NMR apparatus (Karlsruhe, Germany) with a dual-channel 7.0 mm probe. The powder sample was placed in a ZrO_2 rotor with a rotation speed of 6 kHz. The ^{29}Si chemical shift was corrected using an external standard, referenced by DSS (4,4-Dimethyl-4-silapentane-1-sulfonic acid sodium salt) to 1.534 ppm.

3.4. Catalytic Test

Catalytic experiments of ethanol dehydration to ethylene were carried out in a fixed-bed reactor. A quantity of 10 mL of catalyst (40–60 mesh) was placed in a stainless steel tube with an inner diameter of 10 mm. Reactant ethanol (absolute ethanol or 95% ethanol) was injected into the tube by a metering pump at a constant speed, and the reaction temperature was 260–420 °C. Output products were passed through a gas–liquid separator to obtain liquid phase products (including water, ethanol, diethyl ether, and acetaldehyde) and gas phase products (including ethylene, C3 and C4). The product composition was analyzed using a HP-6890 gas chromatograph. Conversion of ethanol, selectivity, and yield were calculated based on the carbon atomic mole number.

4. Conclusions

Among the widely studied catalysts, alumina is the most suitable for industrial ethanol dehydration to ethylene. In order to investigate the influence of crystal surface regulation on surface properties and microstructure of industrial γ-Al_2O_3, γ-Al_2O_3 with the high-energy (111) crystal plane exposed (i.e., HT-γ-Al_2O_3) was synthesized by solvent protection and hydrothermal treatment, and the differences in structural properties between HT-γ-Al_2O_3 and industrial alumina with the thermodynamically stable (110) crystal surface exposed (i.e., C-γ-Al_2O_3) were studied. Catalytic performance of the two catalysts for industrial

ethanol dehydration to ethylene in a fixed-bed reactor was compared. The novel (111) plane-exposed γ-Al_2O_3 showed higher activity, higher selectivity of ethylene, and higher reaction stability. Characterization results indicate that the types and densities of surface OH groups, acid content, and surface interactions are different due to the differences in atomic arrangement and coordination of unsaturated aluminum of different crystal planes. Afterwards, effects of reaction temperature, space velocity, and steam treatment on the performance of HT-γ-Al_2O_3 were investigated. Under the optimal conditions, both the conversion of ethanol and selectivity of ethylene on the HT-γ-Al_2O_3 catalyst were higher than 99%. This work shows the possibility of changing alumina surface properties by crystal plane manipulation and provides a new strategy for further improving the catalytic performance of catalysts for industrial ethanol dehydration to ethylene.

Supplementary Materials: The following supporting information can be downloaded at: https://www.mdpi.com/article/10.3390/catal13060994/s1, Table S1: Calculated surface energies of AlOOH planes. Table S2: Calculated surface energies of γ-alumina planes. Figure S1: Schematic diagram of the corresponding crystal plane changes during the transition of Boehmite to alumina. Figure S2: Selected area electron diffraction (SAED) of (a) HT-γ-Al_2O_3; (b) C-γ-Al_2O_3.

Author Contributions: Conceptualization, J.L., D.W. and W.Y.; Data curation, X.G.; Investigation, X.G.; Methodology, J.L., D.W. and W.D.; Resources, L.P., W.D. and W.Y.; Supervision, W.Y.; Writing—original draft, J.L.; Writing—review and editing, D.W. All authors have read and agreed to the published version of the manuscript.

Funding: This research received no external funding.

Conflicts of Interest: The authors declare no conflict of interest.

References

1. Xiang, N.; Li, S.; Shu, C.; Xu, F. Dynamic material flow analysis of Chinese ethylene production processes and optimal pathway exploration with potential environmental-economic impacts. *J. Clean. Prod.* **2023**, *392*, 136282. [CrossRef]
2. Zhao, Z.; Chong, K.; Jiang, J.; Wilson, K.; Zhang, X.; Wang, F. Low-carbon roadmap of chemical production: A case study of ethylene in China. *Renew. Sustain. Energy Rev.* **2018**, *97*, 580–591. [CrossRef]
3. Walsh, B.; Ciais, P.; Janssens, I.a.; Peñuelas, J.; Riahi, K.; Rydzak, F.; van Vuuren, D.P.; Obersteiner, M. Pathways for balancing CO_2 emissions and sinks. *Nat. Commun.* **2017**, *8*, 14856. [CrossRef]
4. Silva, C.E.F.; Bertucco, A. Bioethanol from microalgae and cyanobacteria: A review and technological outlook. *Process Biochem.* **2016**, *51*, 1833–1842. [CrossRef]
5. Handler, R.; Shonnard, D.R.; Griffing, E.; Lai, A.; Palou-Rivera, I. Life cycle assessments of ethanol production via gas fermentation: Anticipated greenhouse gas emissions for cellulosic and waste gas feedstocks. *Ind. Eng. Chem. Res.* **2015**, *55*, 3253–3261. [CrossRef]
6. Qian, Q.; Cui, M.; He, Z.; Wu, C.; Zhu, Q.; Zhang, Z.; Ma, J.; Yang, G.; Zhang, J.; Han, B. Highly selective hydrogenation of CO_2 into C2+ alcohols by homogeneous catalysis. *Chem. Sci.* **2015**, *6*, 5685–5689. [CrossRef] [PubMed]
7. Luk, H.T.; Mondelli, C.; Ferré, D.C.; Stewart, J.A.; Pérez-Ramírez, J. Status and prospects in higher alcohols synthesis from syngas. *Chem. Soc. Rev.* **2017**, *46*, 1358–1426. [CrossRef]
8. Liu, Y.; Murata, K.; Inaba, M.; Takahara, I. Synthesis of ethanol from methanol and syngas through an indirect route containing methanol dehydrogenation, DME carbonylation, and methyl acetate hydrogenolysis. *Fuel Process. Technol.* **2013**, *110*, 206–213. [CrossRef]
9. Cao, K.; Fan, D.; Gao, M.; Fan, B.; Chen, N.; Wang, L.; Tian, P.; Liu, Z. Recognizing the important role of surface barriers in MOR zeolite catalyzed DME carbonylation reaction. *ACS Catal.* **2022**, *12*, 1–7. [CrossRef]
10. Mohsenzadeh, A.; Zamani, A.; Taherzadeh, M.J. Bioethylene production from ethanol: A review and techno-economical evaluation. *ChemBioEng Rev.* **2017**, *4*, 75–91. [CrossRef]
11. Zhang, M.; Yu, Y. Dehydration of ethanol to ethylene. *Ind. Eng. Chem. Res.* **2013**, *52*, 9505–9514. [CrossRef]
12. Yakovleva, I.S.; Banzaraktsaeva, S.P.; Ovchinnikova, E.V.; Chumachenko, V.A.; Isupova, L.A. Catalytic dehydration of bioethanol to ethylene. *Catal. Ind.* **2016**, *8*, 152–167. [CrossRef]
13. Phung, T.K.; Busca, G. Ethanol dehydration on silica-aluminas: Active sites and ethylene/diethyl ether selectivities. *Catal. Commun.* **2015**, *68*, 110–115. [CrossRef]
14. Wannaborworn, M.; Praserthdam, P.; Jongsomjit, B. A comparative study of solvothermal and sol-gel-derived nanocrystalline alumina catalysts for ethanol dehydration. *J. Nanomater.* **2015**, 519425. [CrossRef]
15. Feng, R.; Yan, X.; Hu, X. Effects of boron and fluorine modified γ-Al_2O_3 with tailored surface acidity on catalytic ethanol dehydration to ethylene. *J. Porous Mater.* **2018**, *25*, 1105–1114. [CrossRef]

16. Janlamool, J.; Jongsomjit, B. Catalytic ethanol dehydration to ethylene over nanocrystalline χ- and γ-Al_2O_3 Catalysts. *J. Oleo Sci.* **2017**, *66*, 1029–1039. [CrossRef]
17. Shetsiri, S.; Thivasasith, A.; Saenluang, K.; Wannapakdee, W.; Salakhum, S.; Wetchasat, P.; Nokbin, S.; Limtrakul, J.; Wattanakit, C. Sustainable production of ethylene from bioethanol over hierarchical ZSM-5 nanosheets. *Sustain. Energy Fuels* **2019**, *3*, 115–126. [CrossRef]
18. Salem, H.M.; Mohamed, R.S.; Alkahlawy, A.A.; Gobara, H.M.; Hassan, A.E.A.; Hassan, S.A. Enhanced ethylene production by dehydration of ethanol over Al/SBA-15 mesoporous catalysts. *J. Porous Mater.* **2019**, *26*, 735–745. [CrossRef]
19. Chen, B.; Lu, J.; Wu, L.; Chao, Z. Dehydration of bio-ethanol to ethylene over iron exchanged HZSM-5. *Chin. J. Catal.* **2016**, *37*, 1941–1948. [CrossRef]
20. Austin, N.; Kostetskyy, P.; Mpourmpakis, G. Design of highly selective ethanol dehydration nanocatalysts for ethylene production. *Nanoscale* **2018**, *10*, 4004–4009. [CrossRef]
21. Xia, W.; Wang, F.; Wang, L.; Wang, J.; Mu, X.; Chen, K. High performance SiO_2-ZrO_2 binary oxide for ethanol conversion to ethylene. *Catal. Lett.* **2018**, *148*, 3024–3034. [CrossRef]
22. Xie, X.; Li, Z.; Li, B.; Wu, X.; An, X. Novel catalyst PTMA-PILC: Structural properties and catalytic performance for the dehydration of bioethanol to ethylene. *RSC Adv.* **2015**, *5*, 46316–46324. [CrossRef]
23. Alharbi, W.; Brown, E.; Kozhevnikova, E.F.; Kozhevnikov, I.V. Dehydration of ethanol over heteropoly acid catalysts in the gas phase. *J. Catal.* **2014**, *319*, 174–181. [CrossRef]
24. Chumachenko, V.A.; Ovchinnikova, E.V. Activities of industrial alumina based catalysts in the dehydration of ethanol to ethylene. *Catal. Ind.* **2016**, *8*, 134–138. [CrossRef]
25. Chaichana, E.; Boonsinvarothai, N.; Chitpong, N.; Jongsomjit, B. Catalytic dehydration of ethanol to ethylene and diethyl ether over alumina catalysts containing different phases with boron modification. *J. Porous Mater.* **2019**, *26*, 599–610. [CrossRef]
26. Phung, T.K.; Lagazzo, A.; Crespo, M.Á.R.; Escribano, V.S.; Busca, G. A study of commercial transition aluminas and of their catalytic activity in the dehydration of ethanol. *J. Catal.* **2014**, *311*, 102–113. [CrossRef]
27. El-Nadjar, W.; Bonne, M.; Trela, E.; Rouleau, L.; Mino, A.; Hocine, S.; Payen, E.; Lancelot, C.; Lamonier, C.; Blanchard, P.; et al. Infrared investigation on surface properties of alumina obtained using recent templating routes. *Microporous Mesoporous Mater.* **2012**, *158*, 88–98. [CrossRef]
28. Feng, R.; Hu, X.; Yan, X.; Yan, Z.; Rood, M.J. A high surface area mesoporous γ-Al_2O_3 with tailoring texture by glucose template for ethanol dehydration to ethylene. *Microporous Mesoporous Mater.* **2016**, *241*, 89–97. [CrossRef]
29. Cai, W.; Zhang, S.; Lv, J.; Chen, J.; Yang, J.; Wang, Y.; Guo, X.; Peng, L.; Ding, W.; Chen, Y.; et al. Nanotubular gamma alumina with high-energy external surfaces: Synthesis and high performance for catalysis. *ACS Catal.* **2017**, *7*, 4083–4092. [CrossRef]
30. Wang, Y.; Yang, J.; Gu, R.; Peng, L.; Guo, X.; Xue, N.; Zhu, Y.; Ding, W. Crystal-facet effect of γ-Al_2O_3 on supporting CrOx for catalytic semihydrogenation of acetylene. *ACS Catal.* **2018**, *8*, 6419–6425. [CrossRef]
31. Cui, Y.; Liu, N.; Xia, Y.; Lv, J.; Zheng, S.; Xue, N.; Peng, L.; Guo, X.; Ding, W. Efficient self-metathesis of 1-butene on molybdenum oxide supported on silica modified one-dimensional γ-Al_2O_3. *J. Mol. Catal. A-Chem.* **2014**, *394*, 1–9. [CrossRef]
32. Ballinger, T.H.; Yates, J.T. IR spectroscopic detection of Lewis acid sites on Al_2O_3 using adsorbed CO. Correlation with Al-OH group removal. *Langmuir* **1991**, *7*, 3041–3045. [CrossRef]
33. Wang, X.; Wovchko, E.A. Infrared spectroscopic investigation of the surface reaction of phosphorus trifluoride on γ-alumina. *Langmuir* **2003**, *19*, 5295–5302. [CrossRef]
34. Knözinger, H.; Ramasamy, P. Catalytic aluminas: Surface models and characterization of surface sites. *Catal. Rev. Sci. Eng.* **1978**, *17*, 31–70. [CrossRef]
35. Morterra, C.; Magnacca, G. A case study: Surface chemistry and surface structure of catalytic aluminas, as studied by vibrational spectroscopy of adsorbed species. *Catal. Today* **1996**, *27*, 497–532. [CrossRef]
36. Krokidis, X.; Raybaud, P.; Gobichon, A.; Rebours, B.; Euzen, P.; Toulhoat, H. Theoretical study of the dehydration process of boehmite to γ-alumina. *J. Phys. Chem. B* **2001**, *105*, 5121–5130. [CrossRef]
37. Ciuparu, D.; Perkins, E.; Pfefferle, L. In situ DR-FTIR investigation of surface hydroxyls on γ-Al_2O_3 supported PdO catalysts during methane combustion. *Appl. Catal. A Gen.* **2004**, *263*, 145–153. [CrossRef]
38. Digne, M.; Sautet, P.; Raybaud, P.; Euzen, P.; Toulhoat, H. Hydroxyl groups on γ-alumina surfaces: A DFT study. *J. Catal.* **2002**, *211*, 1–5. [CrossRef]
39. Digne, M.; Sautet, P.; Raybaud, P.; Euzen, P.; Toulhoat, H. Use of DFT to achieve a rational understanding of acid-basic properties of γ-alumina surfaces. *J. Catal.* **2004**, *226*, 54–68. [CrossRef]
40. Li, X.; Zhang, W.; Liu, S.; Xu, L.; Han, X.; Bao, X. The role of alumina in the supported Mo/HBeta-Al_2O_3 catalyst for olefin metathesis: A high-resolution solid-state NMR and electron microscopy study. *J. Catal.* **2007**, *250*, 55–66. [CrossRef]
41. Gonzales, N.O.; Chakraborty, A.K.; Bell, A.T. A density functional theory study of hydrogen recombination and hydrogen-deuterium exchange on Ga/H-ZSM-5. *Top. Catal.* **1999**, *9*, 207–213. [CrossRef]
42. Phung, T.; Hernández, L.P.; Lagazzo, A.; Busca, G. Dehydration of ethanol over zeolites, silica alumina and alumina: Lewis acidity, Brønsted acidity and confinement effects. *Appl. Catal. A Gen.* **2015**, *493*, 77–89. [CrossRef]
43. Kwak, J.; Mei, D.; Peden, C.; Rousseau, R.; Szanyi, J. (100) facets of γ-Al_2O_3: The active surfaces for alcohol dehydration reactions. *Catal. Lett.* **2011**, *141*, 649–655. [CrossRef]

44. Topchieva, K.V.; Yun-Pin, K.; Smirnova, I.V. 81 Function of surface compounds in the study of catalytic dehydration of alcohols over aluminum oxide and silica-alumina catalysts. *Adv. Catal.* **1957**, *9*, 799–806.
45. DeWilde, J.F.; Chiang, H.; Hickman, D.A.; Ho, C.R.; Bhan, A. Kinetics and mechanism of ethanol dehydration on γ-Al_2O_3: The critical role of dimer inhibition. *ACS Catal.* **2013**, *3*, 798–807. [CrossRef]
46. Kovarik, L.; Genc, A.; Wang, C.; Qiu, A.; Peden, C.H.F.; Szanyi, J.; Kwak, J.H. Tomography and high-resolution electron microscopy study of surfaces and porosity in a plate-like γ-Al_2O_3. *J. Phys. Chem. C* **2013**, *117*, 179–186. [CrossRef]
47. DeWilde, J.F.; Czopinski, C.J.; Bhan, A. Ethanol dehydration and dehydrogenation on γ-Al_2O_3: Mechanism of acetaldehyde formation. *ACS Catal.* **2014**, *4*, 4425–4433. [CrossRef]
48. Ali, S.; Abbas, Y.; Zuhra, Z.; Butler, I.S. Synthesis of γ-alumina (Al_2O_3) nanoparticles and their potential for use as an adsorbent in the removal of methylene blue dye from industrial wastewater. *Nanoscale Adv.* **2019**, *1*, 213–218. [CrossRef]
49. Escribano, V.S.; Garbarino, G.; Finocchio, E.; Busca, G. γ-alumina and amorphous silica-alumina: Structural features, acid sites and the role of adsorbed water. *Top. Catal.* **2017**, *60*, 1554–1564. [CrossRef]
50. Ding, W.; Li, S.; Meitzner, G.D.; Iglesia, E. Methane conversion to aromatics on Mo/H-ZSM5: Structure of molybdenum species in working catalysts. *J. Phys. Chem. B* **2001**, *105*, 506–513. [CrossRef]
51. Xue, N.; Chen, X.; Nie, L.; Guo, X.; Ding, W.; Chen, Y.; Gu, M.; Xie, Z. Understanding the enhancement of catalytic performance for olefin cracking: Hydrothermally stable acids in P/HZSM-5. *J. Catal.* **2007**, *248*, 20–28. [CrossRef]

Disclaimer/Publisher's Note: The statements, opinions and data contained in all publications are solely those of the individual author(s) and contributor(s) and not of MDPI and/or the editor(s). MDPI and/or the editor(s) disclaim responsibility for any injury to people or property resulting from any ideas, methods, instructions or products referred to in the content.